







## Article

# Crystal Engineering of Conglomerates: Dilution of Racemate-Forming Fe(II) and Ni(II) Congeners into Conglomerate-Forming [Zn(bpy)<sub>3</sub>](PF<sub>6</sub>)<sub>2</sub>

Ugo Serdan <sup>1</sup>, Lucas Robin <sup>1</sup>, Mathieu Marchivie <sup>1</sup>, Mathieu Gonidec <sup>1</sup>, Patrick Rosa <sup>1</sup>, Elen Duverger-Nédellec <sup>1</sup>, Emilie Pouget <sup>2</sup>, Philippe Saintavit <sup>3</sup>, Marie-Anne Arrio <sup>3</sup>, Amélie Juhin <sup>3</sup>, Andrei Rogalev <sup>4</sup>, Fabrice Wilhelm <sup>4</sup> and Elizabeth A. Hillard <sup>1,\*</sup>

<sup>1</sup> Univ. Bordeaux, CNRS, Bordeaux INP, ICMCB, UMR 5026, F-33600 Pessac, France

<sup>2</sup> Univ. Bordeaux, CNRS, Bordeaux INP, CBMN, UMR 5248, F-33600 Pessac, France

<sup>3</sup> CNRS, Sorbonne Université, MNHN, IMPMC, UMR 7590, F-75252 Paris, France

<sup>4</sup> European Synchrotron Radiation Facility (ESRF), F-38043 Grenoble, France

\* Correspondence: elizabeth.hillard@icmcb.cnrs.fr

**Abstract:** Conglomerate formation, where enantiomers within a racemic mixture self-segregate upon crystallization, is an advantageous property for obtaining chirally pure crystals and allows large-scale chiral resolution. However, the prevalence of conglomerates is low and difficult to predict. In this report, we describe our attempts to engineer conglomerates from racemate-forming compounds by integrating them into a conglomerate-forming matrix. In this regard, we found that Ni(II) and Fe(II) form molecular alloys with Zn(II) in [M<sub>x</sub>Zn<sub>(1-x)</sub>(bpy)<sub>3</sub>](PF<sub>6</sub>)<sub>2</sub> (where bpy = 2,2'-bipyridyl). Powder X-ray Diffraction (PXRD) and Energy-Dispersive X-ray spectroscopy (EDX) evidenced conglomerate crystallization with Ni(II) concentrations up to about 25%, while it was observed only for much lower concentrations of Fe(II). This can be attributed to the ability of [Ni(bpy)<sub>3</sub>](PF<sub>6</sub>)<sub>2</sub> to access a metastable conglomerate phase, while no such phase has been detected in [Fe(bpy)<sub>3</sub>](PF<sub>6</sub>)<sub>2</sub>. Furthermore, the chiral phase appears to be favored in fast-growing precipitates, while the racemic phase is favored in slow re-crystallizations for both Ni(II) and Fe(II) molecular alloys. X-ray natural circular dichroism (XNCD) measurements on [Ni<sub>0.13</sub>Zn<sub>0.87</sub>(bpy)<sub>3</sub>](PF<sub>6</sub>)<sub>2</sub> demonstrate the chirality of the nickel molecules within the zinc molecular matrix.

**Keywords:** crystal engineering; chirality; conglomerate; molecular alloy; PXRD



**Citation:** Serdan, U.; Robin, L.; Marchivie, M.; Gonidec, M.; Rosa, P.; Duverger-Nédellec, E.; Pouget, E.; Saintavit, P.; Arrio, M.-A.; Juhin, A.; et al. Crystal Engineering of Conglomerates: Dilution of Racemate-Forming Fe(II) and Ni(II) Congeners into Conglomerate-Forming [Zn(bpy)<sub>3</sub>](PF<sub>6</sub>)<sub>2</sub>. *Chemistry* **2023**, *5*, 255–268. <https://doi.org/10.3390/chemistry5010020>

Academic Editors: Zoi Lada and Konstantis Konidaris

Received: 15 December 2022

Revised: 1 February 2023

Accepted: 2 February 2023

Published: 15 February 2023



**Copyright:** © 2023 by the authors. Licensee MDPI, Basel, Switzerland. This article is an open access article distributed under the terms and conditions of the Creative Commons Attribution (CC BY) license (<https://creativecommons.org/licenses/by/4.0/>).

## 1. Introduction

Racemic mixtures of enantiomers crystallize in one of three ways: as racemic crystals containing both enantiomers in equimolar proportions, as solid solutions with the two enantiomers randomly distributed in the crystals, or as conglomerates where the enantiomers self-segregate [1]. While racemic systems and solid solutions are not restrained in terms of space group, conglomerates will necessarily crystallize in one of the 65 non-centrosymmetric Sohncke space groups compatible with chiral enantiopure molecules. While it has been estimated that such spontaneous resolutions occur in only 5–10% of racemic mixtures [2], this feature was central to the discovery of molecular chirality by Louis Pasteur [3] and opens the way to specific chiral purification techniques, such as preferential crystallization [4] or complete deracemization [5], both of which strictly require conglomerate-forming systems. As these methods have been shown to be appropriate for industrial scale-up [6–11], the identification and design of conglomerate systems are of great interest for the enantiopure production of pharmaceuticals, pesticides, etc. Identification methods include the screening of crystallized racemic mixtures for second-harmonic generation (SHG) [12], as well as the construction of phase diagrams from their solubility [1] or melting point [2] data at different enantiomeric enrichments. In particular, the screening of

co-crystals, formed, for example, with solvents [13], other molecules [14] or as salts [15,16], is an important design approach to conglomerate systems.

As conglomerates provide direct access to optically active crystals, they have been used as an alternative to chiral ligands for the design and isolation of chiral metal complexes [17–21]. In the realm of coordination chemistry, octahedral propeller-type complexes are intrinsically chiral and appear to be a particularly rich source of conglomerate-forming compounds [22,23]. As observed in organic co-crystals, the preferential formation of conglomerates is highly dependent on the nature of the counter-ion [24]; for example,  $[\text{Zn}(\text{en})_3](\text{NO}_3)_2$  (where en = ethylenediamine) forms a conglomerate at room temperature [25], while the sulfate salt forms a racemate [26], even if the unit cell and crystal packing are very similar in the two salts.

The formation of conglomerates or racemates can also depend on the metal center. An example of this is the  $[\text{M}(\text{bpy})_3](\text{PF}_6)_2$  family (where bpy = 2,2'-bipyridyl), which crystallizes either in a Sohncke space group as a conglomerate or in a centrosymmetric space group as a racemate, depending on the metal used. For  $[\text{M}(\text{bpy})_3](\text{PF}_6)_2$  where M = divalent manganese [27], technetium [28], cobalt [23,29], copper [30], or zinc [31], a spontaneous resolution of the enantiomers yield crystalline conglomerates in the chiral  $\gamma$ -phase in the enantiomorphic space group pair  $P3_1/P3_2$ . On the other hand, when M = divalent iron [32], ruthenium [31,33–35], or osmium [36,37], the compounds crystallize as racemates in the centrosymmetric  $\beta$ -phase ( $P\bar{3}c1$ ) and may undergo a low-temperature phase transition to the non-centrosymmetric space group  $P3c1$  [38]. The nickel(II) derivative  $[\text{Ni}(\text{bpy})_3](\text{PF}_6)_2$  represents an intermediate case; this compound has been reported in both the  $\gamma$ -phase [39] and the  $\beta$ -phase [35,40], with both appearing concomitantly in the same crystallization batch [31]. The simultaneous appearance of both phases suggests that the energies are similar, and Breu et al. identified the racemic  $\beta$ -phase of  $[\text{Ni}(\text{bpy})_3](\text{PF}_6)_2$  as the thermodynamic phase, stabilized by 5.4 kJ/mol compared to the conglomerate  $\gamma$ -phase [41].

In order to broaden access to conglomerate systems, the current work describes attempts to induce spontaneous resolution of  $[\text{Fe}(\text{bpy})_3](\text{PF}_6)_2$  and  $[\text{Ni}(\text{bpy})_3](\text{PF}_6)_2$  by associating these molecules with  $[\text{Zn}(\text{bpy})_3](\text{PF}_6)_2$  as a conglomerate-forming matrix. While the formation of alloys has been known for millennia, the formation of molecular solid solutions or “molecular alloys” [35] has been more rarely used to improve the physical properties of materials and typically involves the co-crystallization of isostructural compounds. Examples of molecular alloys using molecular congeners can be especially found in the molecular magnetism community, where magnetic relaxation may be slowed by the isolation of single-molecule magnets within a diamagnetic matrix [42,43]. The imposition of a different crystalline structure on one of the components of a molecular alloy is, however, rather uncommon. We note particularly the thesis work by M.C. Balogh, who found that it was possible to impose the structure of the dominant compound on the minority compound in the context of lanthanide tris-dipicolinate guanidinium complexes [44].

In the present work, binary mixtures of  $[\text{Fe}(\text{bpy})_3](\text{PF}_6)_2$  or  $[\text{Ni}(\text{bpy})_3](\text{PF}_6)_2$  with the zinc analogue were evaluated both as precipitates immediately formed upon the mixture of the reagents, and again after recrystallization, to try to differentiate between potential kinetic and thermodynamic phases. Single-crystal X-ray diffraction (SCXRD), powder X-ray diffraction (PXRD), and energy-dispersive X-ray spectroscopy (EDX) data suggest that it is indeed possible to isolate  $[\text{Ni}_x\text{Zn}_{(1-x)}(\text{bpy})_3](\text{PF}_6)_2$  in conglomerate form, but that the proportion of  $[\text{Fe}(\text{bpy})_3](\text{PF}_6)_2$  that could be introduced into the conglomerate matrix appeared to be very limited, although non-zero. The high solubility of the nickel congener in the zinc matrix allowed the demonstration of optical activity using X-rays at the Ni K-edge, while the iron incorporation was too low to clearly evidence a chiral response, even if the visual inspection of individual crystals suggests that the iron partially exists in the conglomerate phase.

## 2. Materials and Methods

All syntheses were performed at room temperature under an ambient atmosphere. The metal sulfates,  $\text{KPF}_6$ , 2,2'-bipyridine and organic solvents were obtained commercially and used as received. Water was deionized using an ion-exchange resin to reach a resistivity of  $\geq 10 \text{ M}\Omega\cdot\text{cm}$ .

### 2.1. General Procedure for $[\text{M}(\text{bpy})_3](\text{PF}_6)_2$

$\text{MSO}_4\cdot n\text{H}_2\text{O}$  (1 mmol, Table 1) was dissolved in 5 mL of water,  $\text{KPF}_6$  (3 mmol, 0.552 g) was dissolved in 10 mL of water, and 2,2'-bipyridine (4 mmol, 0.625 g) was dissolved in 12.5 mL of an EtOH/water mixture (4:1). The bpy solution was added to the metallic one and stirred 10 min. The product was precipitated in quantitative yield by dropwise addition of the  $\text{KPF}_6$  solution. The precipitate was isolated by filtration on type 4 sintered glass and washed three times with distilled water and twice with absolute ethanol and dried in the air for one day.

**Table 1.** Masses of metal sulfates used in the synthesis of pure  $[\text{M}(\text{bpy})_3](\text{PF}_6)_2$  compounds.

Compound	$\text{MSO}_4\cdot n\text{H}_2\text{O}$	Mass $\text{MSO}_4\cdot n\text{H}_2\text{O}$
$[\text{Mn}(\text{bpy})_3](\text{PF}_6)_2$	$\text{MnSO}_4\cdot\text{H}_2\text{O}$	0.169 g
$[\text{Fe}(\text{bpy})_3](\text{PF}_6)_2$	$\text{FeSO}_4\cdot 7\text{H}_2\text{O}$	0.278 g
$[\text{Co}(\text{bpy})_3](\text{PF}_6)_2$	$\text{CoSO}_4\cdot 7\text{H}_2\text{O}$	0.281 g
$[\text{Cu}(\text{bpy})_3](\text{PF}_6)_2$	$\text{CuSO}_4\cdot 5\text{H}_2\text{O}$	0.250 g
$[\text{Ni}(\text{bpy})_3](\text{PF}_6)_2$	$\text{NiSO}_4\cdot 7\text{H}_2\text{O}$	0.281 g
$[\text{Zn}(\text{bpy})_3](\text{PF}_6)_2$	$\text{ZnSO}_4\cdot 7\text{H}_2\text{O}$	0.288 g

The powders were re-crystallized by dissolving about 250 mg of powder in acetone, acetonitrile, or dichloromethane under stirring. The solutions were filtered using a syringe fitted with a  $0.22 \mu\text{m}$  porosity filter to remove undissolved powders. The solutions were placed in vials loosely closed with a screw cap, allowing the solvent to evaporate slowly. The crystals were selected, and their unit cell was determined using SCXRD (Table S3). In the case of  $[\text{Ni}(\text{bpy})_3](\text{PF}_6)_2$ , crystals formed by vapor diffusion of diethylether into an acetonitrile solution were also ground with a mortar and pestle and examined by PXRD.

### 2.2. General Procedure for $[\text{M}_x\text{Zn}_{(1-x)}(\text{bpy})_3](\text{PF}_6)_2$

$[\text{M}_x\text{Zn}_{(1-x)}(\text{bpy})_3](\text{PF}_6)_2$  was prepared as above, but instead of using a pure metal sulfate,  $\text{ZnSO}_4\cdot 7\text{H}_2\text{O}$  and  $\text{NiSO}_4\cdot 7\text{H}_2\text{O}$  or  $\text{FeSO}_4\cdot 7\text{H}_2\text{O}$  were dissolved together in 5 mL of water (Table 2). The powders of the molecular alloys were recrystallized by vapor diffusion of diethyl ether into an acetonitrile solution.

### 2.3. X-ray Diffraction

Crystals of  $[\text{Ni}(\text{bpy})_3](\text{PF}_6)_2$  and  $[\text{Zn}(\text{bpy})_3](\text{PF}_6)_2$  suitable for X-ray diffraction were selected in ambient conditions and attached to a MiTeGen microloop with silicone grease. The crystals were mounted at 298(2) K and centered in the X-ray beam using a video camera. Data collections were performed with Mo  $\text{K}\alpha$  ( $\lambda = 0.71073 \text{ \AA}$ ) radiation on a Bruker Kappa APEXII, operating at 50 kV and 30 mA using graphite monochromated radiation. The data were collected using a routine to survey reciprocal space, and reduction was performed using software included in the Bruker Apex4 suite [45]. The structures were solved using direct methods [46]. Non-hydrogen atoms were refined anisotropically using weighted full-matrix least-squares on  $F^2$ , followed by difference Fourier synthesis [47,48]. All hydrogen atoms were included in the final structure factor calculation at idealized positions and were allowed to ride on the neighboring atoms with relative isotropic displacement coefficients. Data for the compounds in Table S2 were obtained similarly, although here only enough data to determine the unit cell parameters were collected.

**Table 2.** Quantities of metal sulfates used in the synthesis of  $M_xZn_{(1-x)}(bpy)_3](PF_6)_2$  molecular alloys.

mmol $NiSO_4 \cdot 7H_2O$	mmol $ZnSO_4 \cdot 7H_2O$	Mass $ZnSO_4 \cdot 7H_2O$	Mass $NiSO_4 \cdot 7H_2O$
0.1	0.9	0.259 g	0.028 g
0.2	0.8	0.230 g	0.056 g
0.3	0.7	0.201 g	0.084 g
0.4	0.6	0.173 g	0.112 g
0.5	0.5	0.144 g	0.140 g
0.6	0.4	0.115 g	0.169 g
0.7	0.3	0.086 g	0.197 g
0.8	0.2	0.058 g	0.225 g
0.9	0.1	0.029 g	0.253 g
mmol $FeSO_4 \cdot 7H_2O$	mmol $ZnSO_4 \cdot 7H_2O$	Mass $ZnSO_4 \cdot 7H_2O$	Mass $FeSO_4 \cdot 7H_2O$
0.1	0.9	0.259 g	0.028 g
0.2	0.8	0.230 g	0.056 g
0.3	0.7	0.201 g	0.083 g
0.4	0.6	0.173 g	0.111 g
0.5	0.5	0.144 g	0.139 g

Powder X-ray diffraction data of precipitates were recorded using a PANalytical X'Pert PRO MPD diffractometer with Bragg–Brentano geometry,  $Cu-K\alpha_{1,2}$  radiation ( $\lambda = 1.54184 \text{ \AA}$ ) and a graphite backscattering monochromator, using standard Al sample holders. Powder X-ray diffraction of ground crystals was performed on 0.3 mm diameter glass capillaries in transmission geometry using a Bruker D8 Mo- $K\alpha_{1,2}$  radiation ( $\lambda = 0.71075 \text{ \AA}$ ) diffractometer. The Debye–Scherrer setup employed a focusing Göbel mirror primary optic, with  $2.5^\circ$  primary and secondary Soller slits and a Dectris EIGER2R-500K detector performing 1D mode  $2\theta$  scans in 158 min, over the range  $2\text{--}25^\circ$ , with a  $0.02^\circ$   $2\theta$  step size. Le Bail and Reitveld refinements were performed with JANA2020 [49].

#### 2.4. IR Spectroscopy

Infrared spectra on precipitated powders of the compounds were obtained on an IRAffinity-1 (Shimadzu) Fourier Transform Infrared Spectrophotometer, equipped with MIRacle 10 single reflection ATR module (Pike Technologies); 512 scans accumulated.

#### 2.5. EDX

Energy-dispersive X-ray spectroscopy was performed on a JEOL 6360A Scanning Electron Microscope equipped with an EDX detector. The crystals were mounted on the sample holder by affixing them on conductive carbon adhesive tape, and to prevent charging during the analyses, the sample was sputter-coated by a thin film of Au. The spectra were acquired at an acceleration voltage of 20 keV unless specified otherwise. The quantitative analysis was performed directly with JEOL's Analysis Station software using the Phi-Rho-Z method on the  $K\alpha$  lines of the transition metal elements.

#### 2.6. XNCD

X-ray absorption experiments at the Ni and Fe K-edges were carried out at the ID12 beamline of the European Synchrotron Radiation Facility (Grenoble, France), dedicated to polarization-dependent X-ray spectroscopy in the 2–15 keV energy range. A high flux of circularly polarized photons was provided by a HELIOS-II undulator. X-rays were monochromatized by a Si(111) double-crystal monochromator. For XNCD studies, the samples were glued with a carbon tape pad on an aluminum sample holder and oriented so that the crystal's *c*-axis and the photons wave vector formed an angle of  $90^\circ$  (Figure S6). All spectra were recorded at room temperature in total X-ray fluorescence yield detection mode in backscattering geometry. At the Ni K-edge, sets of absorption spectra were acquired, alternating the photon helicity after each spectrum 8 times, for a total of 16 spectra. The spectra were then normalized with reference points at the pre-edge (8320 eV) and post-edge

(8398 eV). The absorption spectrum was obtained by averaging all normalized spectra, and XNCD was obtained by averaging the difference of the 8 sets of dichroic pairs. At the Fe K-edge, spectra were marred with intense diffraction peaks from the sample, which prevented a correct treatment. The only pair of spectra partially exploitable was normalized at the pre-edge (7105 eV) and post-edge (7192.3 eV).

### 3. Results and Discussion

#### 3.1. Phase Determination of Pure $[M(\text{bpy})_3](\text{PF}_6)_2$ in Powders and Crystals

Polycrystalline samples of  $[M(\text{bpy})_3](\text{PF}_6)_2$ , where M = Mn(II), Fe(II), Co(II), Ni(II), Cu(II), and Zn(II), were prepared by rapid precipitation by adding an aqueous solution of  $\text{KPF}_6$  to an EtOH/water mixture of 2,2'-bipyridine and the metal sulfate. Le Bail refinement of PXRD data from the precipitates was performed using representative  $\gamma$ -phase (WOTSON) and  $\beta$ -phase (WOTSAZ or NUZKOI) structures found in the Cambridge Structural Database (CSD) [50]. In the case of  $[\text{Mn}(\text{bpy})_3](\text{PF}_6)_2$ , refinements of two different synthesis batches both showed the presence of significant unidentified impurities in addition to the chiral  $\gamma$ -phase. The powders of the other complexes were monophasic and adopted the conglomerate  $\gamma$ -phase, except for  $[\text{Fe}(\text{bpy})_3](\text{PF}_6)_2$ , which was found to be wholly in the racemic  $\beta$ -phase (Table 3). While both the crystalline  $\gamma$ - and  $\beta$ -phase for  $[\text{Ni}(\text{bpy})_3](\text{PF}_6)_2$  have been reported in the literature [31,35,39,40], under the present conditions of rapid precipitation, only the  $\gamma$ -phase was obtained.

**Table 3.** Le Bail refinements for  $[M(\text{bpy})_3](\text{PF}_6)_2$  precipitates.

Metal	Phase	$a$ (Å)	$c$ (Å)	$V$ (Å <sup>3</sup> )	GOF	$V$ (Å <sup>3</sup> ) SC <sup>a</sup>
Fe	$\beta$	10.6392(11)	16.588(3)	1626.1(4)	1.46	1561.3
Co	$\gamma$	10.4818(9)	26.525(3)	2523.9(5)	1.24	2432.0
Ni	$\gamma$	10.5058(11)	26.367(4)	2520.3(5)	1.48	2415.8
Cu	$\gamma$	10.4921(13)	26.428(4)	2519.6(7)	1.72	2482.1
Zn	$\gamma$	10.5046(9)	26.455(3)	2528.1(4)	1.52	2507.9

<sup>a</sup> Single-crystal data; the cell volumes found by Le Bail refinement are consistently too large, by a maximum of 4.3% compared to single-crystal data.

The powders were re-crystallized by using various methods, and the unit cell parameters of the selected crystals were determined by using single-crystal X-ray diffraction (Table S2). The data show that the Co(II), Cu(II), Mn(II), and Zn(II) compounds tend to form conglomerates, while the Fe(II) and Ni(II) compounds tend to form racemic crystals. This is consistent with literature reports [23,27,29,31], except that, in the present conditions, no conglomerate  $\gamma$ - $[\text{Ni}(\text{bpy})_3](\text{PF}_6)_2$  crystals were observed, as further confirmed from the PXRD data conducted on a ground batch of  $[\text{Ni}(\text{bpy})_3](\text{PF}_6)_2$  crystals (Figure S1). On the other hand, the chiral  $\gamma$ -phase of  $[\text{Ni}(\text{bpy})_3](\text{PF}_6)_2$  was the only one obtained upon rapid precipitation, which supports the interpretation that the  $\beta$ -phase is the thermodynamic phase, while the  $\gamma$ -phase is the kinetic phase [41].

Infrared spectra were obtained for powders of all of the compounds. Very small differences between the conglomerate and racemic phases can be observed, as pointed out by the asterisks in Figure S2. We note the appearance of a peak at 1598–1602  $\text{cm}^{-1}$  that appears in the conglomerate powders but not in the racemic iron system, as well as two peaks around 1010–1023  $\text{cm}^{-1}$  and another set of two peaks around 653–630  $\text{cm}^{-1}$ . While it appears possible to differentiate the two phases using infrared spectroscopy, further experimental and theoretical work will have to be undertaken to use this technique to quantitatively evaluate phase mixtures.

Concerning the preference for the conglomerate or racemic phase in the series of  $[M(\text{bpy})_3](\text{PF}_6)_2$  molecules, we note that the preferred phase appears to be correlated to the average M–N distances. In the case of  $[\text{Ni}(\text{bpy})_3](\text{PF}_6)_2$ , the packing appears to dictate the M–N distances, longer by ca. 0.02 Å in the  $\gamma$ -phase than in the  $\beta$ -phase (Table 4).

**Table 4.**  $[M(\text{bpy})_3](\text{PF}_6)_2$  compounds organized by average M–N distance.

	M(II)	T	$[M-N]_{\text{avg}}$ (Å)	Ref.
Racemic $\beta$ -phase	Fe	rt	1.967	[32]
	Ru	rt	2.055	[33]
	Os	rt	2.056	[36]
	Ni	rt	2.078	[40]
	Tc	rt	2.076(2)	This work <sup>a</sup>
			2.076	[28]
Chiral $\gamma$ -phase	Ni	rt	2.090	[39]
	Cu	rt	2.119	[30]
	Co	rt	2.142	[23]
	Zn	rt	2.159(5)	This work <sup>a</sup>
	Mn	rt	2.249	[27]
	Cd	223 K	2.335	[51]

<sup>a</sup> see Table S1 for crystallographic information.

For this analysis, we obtained room temperature crystal structures of *rac*- $[\text{Ni}(\text{bpy})_3](\text{PF}_6)_2$  and  $[\Lambda\text{-Zn}(\text{bpy})_3](\text{PF}_6)_2$ . Bond distances for *rac*- $[\text{Ni}(\text{bpy})_3](\text{PF}_6)_2$  at 295 K were published in reference [40], but atomic positions are not available on the Cambridge Structural Database, hence the redetermination. Crystallographic information can be found in Table S1, and the structures are shown in Figure 1. As previously observed [31], the packing of the two phases shows significant differences, dominated by T-type  $\pi$ -stacking in the racemate and by co-planar  $\pi$ -stacking in the conglomerate. Likewise, as previously reported,  $[\Lambda\text{-Zn}(\text{bpy})_3](\text{PF}_6)_2$  crystallizing in space group  $P3_2$  suffered from significant merohedral twinning, which was resolved using the twin law reported by Breu et al. [31].

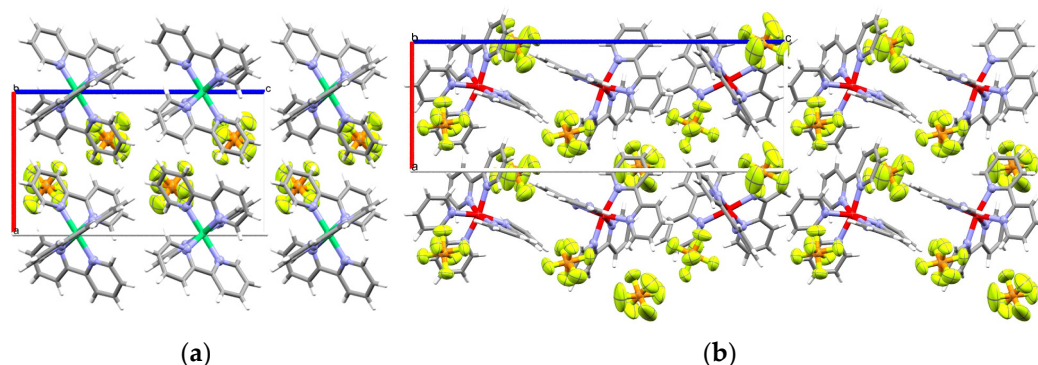


**Figure 1.** Diagrams of (a)  $[\text{rac-Ni}(\text{bpy})_3](\text{PF}_6)_2$  and (b)  $[\Lambda\text{-Zn}(\text{bpy})_3](\text{PF}_6)_2$  from X-ray diffraction. C gray; H white; N lavender; Ni green; Zn red. Ellipsoids of non-C non-H shown at 50% probability level.

### 3.2. Molecular Alloys of $[\text{Ni}_x\text{Zn}_{(1-x)}(\text{bpy})_3](\text{PF}_6)_2$

Powders were prepared by combining a specific ratio of  $\text{ZnSO}_4 \cdot 7\text{H}_2\text{O}$  with  $\text{NiSO}_4 \cdot 7\text{H}_2\text{O}$  in water/EtOH in the presence of bipyridine, followed by precipitation with  $\text{KPF}_6$ , using the same protocol as previously. As expected from the previous observation of the  $\gamma$ -phase in both  $[\text{Ni}(\text{bpy})_3](\text{PF}_6)_2$  and  $[\text{Zn}(\text{bpy})_3](\text{PF}_6)_2$  under the same conditions, PXRD of the precipitates ranging from 90% molar mass of  $[\text{Zn}(\text{bpy})_3](\text{PF}_6)_2$  to 80%  $[\text{Ni}(\text{bpy})_3](\text{PF}_6)_2$  show that all of the samples adopt this chiral phase (Table 5, Figure S3). The unit cell parameters tend to decrease with increasing Ni(II), which is consistent with the slightly smaller volume found in the previous refinement for the Ni(II) pure compound compared to that of the Zn(II) one, 2520.3(5) vs. 2528.1(4) Å<sup>3</sup>, respectively.

**Table 5.** Le Bail refinements for co-precipitations of  $[\text{Ni}(\text{bpy})_3](\text{PF}_6)_2$  with  $[\text{Zn}(\text{bpy})_3](\text{PF}_6)_2$  <sup>a</sup>.

Ni (mol %)	<i>a</i> (Å)	<i>c</i> (Å)	<i>V</i> (Å <sup>3</sup> )	GOF
10	10.5022(5)	26.453(1)	2526.8(2)	1.37
20	10.4978(5)	26.457(2)	2525.0(3)	1.37
30	10.4953(5)	26.447(1)	2522.9(2)	1.34
40	10.4969(5)	26.443(2)	2523.3(2)	1.41
60	10.4964(5)	26.440(2)	2522.8(3)	1.41
70	10.4965(5)	26.430(2)	2521.9(2)	1.54
80	10.4932(5)	26.419(2)	2519.2(2)	1.54

<sup>a</sup> The refinements of the powders prepared with proportions of 50% and 90% Ni gave poor GOFs due to misalignment of the sample as observed by a displacement of the Al sample holder peaks, and these data have thus been omitted.

In an attempt to obtain  $\gamma$ - $[\text{Ni}_x\text{Zn}_{(1-x)}(\text{bpy})_3](\text{PF}_6)_2$  as single crystals, the powders were re-crystallized through the vapor diffusion of diethyl ether into acetonitrile solutions. Notably, different crystal forms were observed depending on the proportion of Ni(II) used in the reaction: needles with 10% of Ni(II) and a mixture of needles and plates with equimolar proportions of Zn(II) and Ni(II) (Figure 2). SCXRD unit cell determination of selected crystals showed that needles are indicative of the conglomerate phase and the plates represent the racemic phase, while a visual inspection of the color of the two crystals indicates the presence of  $[\text{Ni}(\text{bpy})_3](\text{PF}_6)_2$  in both phases.



**Figure 2.** Photos of crystals obtained from the recrystallization of powders of  $[\text{Ni}_x\text{Zn}_{(1-x)}(\text{bpy})_3](\text{PF}_6)_2$ : (a) 10% Ni and 90% Zn (needles); (b) 50% Ni and 50% Zn (needles + plates). Vials shown are 13 mm in diameter.

The bulk crystals were ground in a mortar and measured by PXRD to determine the proportion of the two phases as a function of Ni(II) content. Here, one sees the tendency of crystalline  $[\text{Ni}(\text{bpy})_3](\text{PF}_6)_2$  to favor the racemic  $\beta$ -phase more than the powder form, but also its ability to integrate into the conglomerate matrix: with 10–20% of nickel, only the chiral  $\gamma$ -phase was observed; with 30–50% of nickel, both phases are observed, and at 60%–90% of nickel, only the racemic  $\beta$ -phase is observed (Table 6, Figure S4). The lack of any racemic phase at low Ni(II) proportions, and the lack of any conglomerate phase at high proportions, indicates that the metal complexes efficiently co-crystallize to form molecular alloys and adopt the phase of the prevailing metal. At 30% to 50% of Ni(II), the proportion of the  $\beta$ -phase is found to be higher than that of the Ni(II) concentration, suggesting the presence of a number of racemic zinc-containing crystals and a limit to the  $[\text{Ni}(\text{bpy})_3](\text{PF}_6)_2$  solubility in the conglomerate matrix.

**Table 6.** Rietveld refinements of co-crystallizations of  $[\text{Ni}(\text{bpy})_3](\text{PF}_6)_2$  with  $[\text{Zn}(\text{bpy})_3](\text{PF}_6)_2$ .

Ni(II) (mol %)	$\beta$ -Phase (%)	$a_\gamma$ (Å)	$c_\gamma$ (Å)	$v_\gamma$ (Å <sup>3</sup> )	$a_\beta$ (Å)	$c_\beta$ (Å)	$v_\beta$ (Å <sup>3</sup> )
10	0	10.479(1)	26.402(6)	2510.6(5)	–	–	–
20	0 <sup>a</sup>	10.475(1)	26.393(6)	2508.3(5)	–	–	–
30	45	10.478(2)	26.400(12)	2510(1)	10.796(3)	16.570(8)	1673(1)
40	57	10.477(4)	26.395(17)	2509(1)	10.787(3)	16.562(8)	1669(2)
50	56	10.477(3)	26.402(12)	2510(1)	10.780(2)	16.564(6)	1667(1)
60	100 <sup>b</sup>	–	–	–	10.777(2)	16.571(6)	1666.7(5)
70	100	–	–	–	10.770(2)	16.562(6)	1663.8(5)
80	100	–	–	–	10.769(2)	16.569(6)	1664.2(5)
90	100	–	–	–	10.759(2)	16.564(6)	1660.6(5)

<sup>a</sup> Trace of  $\beta$  phase. <sup>b</sup> Trace of  $\gamma$  phase.

According to the found refined parameters, only the  $\beta$  phase is significantly affected by the Ni ratio as the unit cell volume quasi-linearly decreases from 1673 Å<sup>3</sup> for 30% of Ni to 1661 Å<sup>3</sup> for 90% of Ni, in line with the smaller size of the Ni(II) cation vs. Zn(II). The incorporation of Ni(II) may be thus relatively low in the  $\gamma$  phase while significant in the  $\beta$  phase. However, as the racemic  $\beta$ -phase only appears at 30% Ni, we can assume that the proportion of Ni(II) in the conglomerate  $\gamma$ -phase can reach at least 20%.

### 3.3. Molecular Alloys of $[\text{Fe}_x\text{Zn}_{(1-x)}(\text{bpy})_3](\text{PF}_6)_2$

Powders with proportions of Fe(II) ranging from 10% to 50% were formed in the same way as the nickel-based molecular alloys. At all concentrations, a mixture of the two phases could be identified in the PXRD data (Table 7, Figure S5). In general, the proportion of the  $\beta$ -phase tends to be lower than the starting iron concentrations, which suggests that some of the iron can be incorporated into the zinc matrix to crystallize in the conglomerate form, which is in line with the decrease in the unit cell volume of the  $\gamma$  phase up to 30% Fe(II). Above 30%, the racemic  $\beta$  phase proportion significantly increases, while the  $\beta$  and  $\gamma$  cell parameters remain almost unchanged. It is then probable that the  $\beta$  phase contains essentially Fe(II) and very little Zn(II).

**Table 7.** Rietveld refinements of co-precipitations of  $[\text{Fe}(\text{bpy})_3](\text{PF}_6)_2$  with  $[\text{Zn}(\text{bpy})_3](\text{PF}_6)_2$ .

Fe(II) (mol %)	$\beta$ -Phase (%)	$a_\gamma$ (Å)	$c_\gamma$ (Å)	$v_\gamma$ (Å <sup>3</sup> )	$a_\beta$ (Å)	$c_\beta$ (Å)	$v_\beta$ (Å <sup>3</sup> )
10	1	10.500(4)	26.426(12)	2523(2)	10.74	16.59	1657
20	4	10.498(4)	26.417(13)	2521(2)	10.741(21)	16.587(49)	1657(2)
30	12	10.497(4)	26.385(14)	2518(2)	10.752(4)	16.582(12)	1660(2)
40	27	10.497(4)	26.373(13)	2517(2)	10.754(5)	16.582(13)	1660(2)
50	65	10.504(5)	26.346(17)	2517(2)	10.753(4)	16.584(9)	1661(2)

The precipitates were subsequently recrystallized from acetonitrile and diethyl ether. They showed two distinct forms: large ruby-red needles in the conglomerate phase and very dark small needles in the racemic phase (Figure 3). In some crystals, dark domains could be discerned in the red conglomerate crystals. This system thus appears to be heterogeneous both within and among the crystals.





**Figure 3.** Photo of crystals obtained from the recrystallization of  $[\text{Fe}_{0.4}\text{Zn}_{0.6}(\text{bpy})_3](\text{PF}_6)_2$ . Dark needles = racemic crystals, ruby needles = conglomerate crystals.

As precipitates, the conglomerate phase of  $[\text{Fe}_x\text{Zn}_{(1-x)}(\text{bpy})_3](\text{PF}_6)_2$  was generally favored, while after the growth of single crystals, the proportions of the racemic phase tend to be higher than the starting iron quantity (Table 8, Figure S5). This is the same trend as seen in the Ni(II) experiments (Table 6), showing the increased prevalence of the  $\beta$ -phase after slow crystallization. The evolution of the unit cell volume in the  $\beta$ -phase is consistent with the proportion of iron used in the sample preparations, while, as previously, the conglomerate  $\gamma$ -phase does not show large changes, meaning that the  $\gamma$ -phase probably contains a very limited amount of iron. The strong deviations at 30% and 40% observed in the phase ratio are likely due to an unrepresentative sampling of the crystals due to the heterogeneity of the sample. As previously observed for the powder samples, it seems that the racemic  $\beta$  phase is mostly constituted of the Fe compound.

**Table 8.** Reitveld refinements for co-crystallizations of  $[\text{Fe}(\text{bpy})_3](\text{PF}_6)_2$  with  $[\text{Zn}(\text{bpy})_3](\text{PF}_6)_2$ .

Fe(II) (mol %)	$\beta$ -Phase (%)	$a_\gamma$ (Å)	$c_\gamma$ (Å)	$v_\gamma$ (Å <sup>3</sup> )	$a_\beta$ (Å)	$c_\beta$ (Å)	$v_\beta$ (Å <sup>3</sup> )
10	7	10.476(2)	26.393(8)	2509(1)	10.706(11)	16.517(28)	1639(1)
20	29	10.476(3)	26.395(10)	2509(2)	10.666(4)	16.539(11)	1629(1)
30	59	10.478(6)	26.380(20)	2508(3)	10.644(4)	16.533(11)	1622(2)
40	90	10.476(10)	26.310(43)	2500(4)	10.632(3)	16.533(7)	1619(4)
50	54	10.477(4)	26.384(13)	2508(2)	10.630(3)	16.536(8)	1618(2)

### 3.4. EDX

While the presence of nickel or iron compounds in the crystals could be confirmed by visual inspection of the color (Figures 2 and 3), the quantitative proportions of the metals in individual crystals are unknown. Using EDX, 46 crystals of  $[\text{Ni}_x\text{Zn}_{(1-x)}(\text{bpy})_3](\text{PF}_6)_2$  prepared with 40% Ni(II) and 60% Zn(II) as well as 48 crystals of  $[\text{Fe}_x\text{Zn}_{(1-x)}(\text{bpy})_3](\text{PF}_6)_2$  prepared with 50% Fe(II) and 50% Zn(II), of unknown phase were assayed. The average value over the entire collection of crystals was found to be 40.8% nickel and 52.2% iron, respectively, consistent with the starting proportion of the metals. As indicated in Figure 4, the crystal batch of  $[\text{Ni}_x\text{Zn}_{(1-x)}(\text{bpy})_3](\text{PF}_6)_2$  was relatively homogenous, with 65% of the crystals containing between 30 and 50% Ni and 35% outside of these values. Indeed, all of the assayed crystals possessed both Ni(II) and Zn(II) in significant quantities. We then selected crystals from various batches of different initial compositions, for which the phase was first determined by SCXRD, and the proportion of metals was assayed by EDX (Table 9). Among this small sampling, the crystals found in the  $\gamma$ -phase possessed a maximum of ca. 24% Ni (Table 9), which shows that Ni(II) can be incorporated in rather high proportions while still retaining the conglomerate phase, in accordance with the observations from the PXRD data (c.f. Table 6).

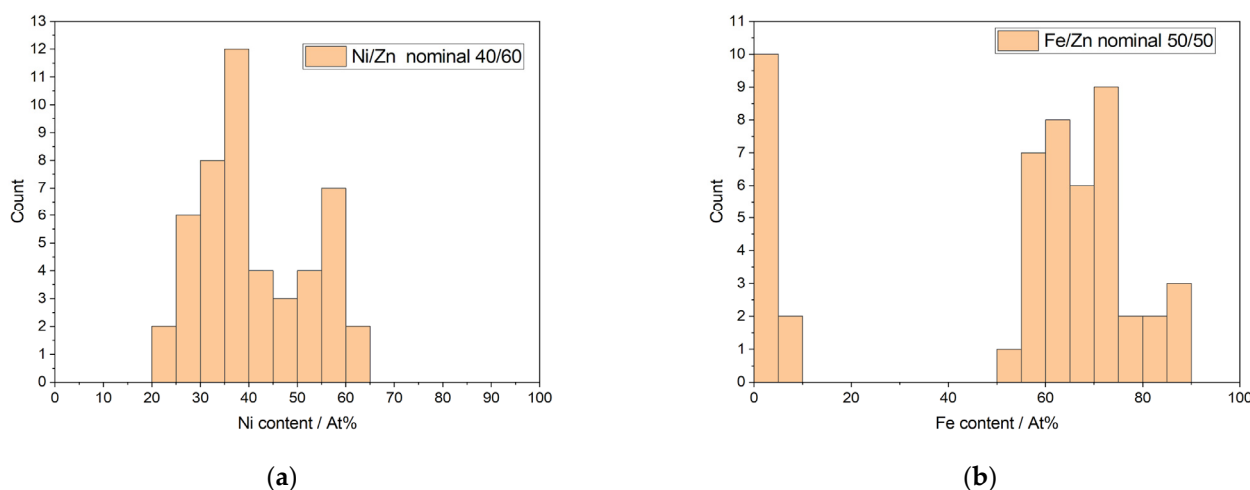


Figure 4. (a) Ni content of 48 crystals, and (b) Fe content of 49 crystals, as determined by EDX.

Table 9. Metal assay by EDX of  $[M_xZn_{(1-x)}(bpy)_3](PF_6)_2$  according to metal proportion and phase.

Theoretical		Found		Phase	Theoretical		Found		Phase
Ni (%)	Zn (%)	Ni (%)	Zn(%)		Fe (%)	Zn (%)	Fe (%)	Zn (%)	
10	90	10.6	89.4	$\gamma$	10	90	2.4	97.6	$\gamma$
30	70	24.4	75.6	$\gamma$	20	80	2.5	97.5	$\gamma$
50	50	9.1	90.9	$\gamma$	30	70	1.4	98.6	$\gamma$
50	50	54.3	45.7	$\beta$	30	70	1.4	98.6	$\gamma$
60	40	66.6	33.4	$\beta$	30	70	86.2	13.8	$\beta$
90	10	95.5	4.5	$\beta$	40	60	61.3	38.7	$\beta$
90	10	94.9	5.1	$\beta$	40	60	2.2	97.8	$\gamma$

Performing the same sampling in the case of iron, any conglomerates were always found with very low quantities of iron, with a maximum of 2.5% (Table 9), in full agreement with PRXD results on ground single crystals. EDX measurements on a collection of 49 crystals yielded a stark bimodal distribution: some crystals were low in iron, which likely corresponds to conglomerates, while another group was found to have a majority of iron, which likely corresponds to the racemic crystals (Figure 3 and ESI Figure S6a,b).

These data, taken together, show very different behaviors in the nickel molecular alloys vs. the iron molecular alloys. The fact that the  $\beta$ -phase is present even with very low Fe(II) concentrations shows the strong propensity of  $[Fe(bpy)_3](PF_6)_2$  to crystallize as a racemate. Indeed, molecular alloys of  $[Fe_xZn_{(1-x)}(bpy)_3](PF_6)_2$  tend to be mainly zinc-based conglomerates or iron-based racemates (Table 9). The iron and zinc compounds have limited miscibility, with the highest Fe(II) proportions found in a conglomerate crystal being 6.1% (Figure S7, crystal phase determined by SCXRD). This induced us to limit our syntheses to an equimolar ratio of iron and zinc, as increasing the starting concentration of iron did not appear to improve the proportion of iron found in the conglomerate crystals.  $[Ni(bpy)_3](PF_6)_2$ , on the other hand, tends to crystallize within the  $[Zn(bpy)_3](PF_6)_2$  matrix in a wide range of proportions (Figure 4a). While higher Ni(II) concentrations tend to favor racemates, at least 24.4% of nickel can be integrated into conglomerate crystals. EDX measurements show that the quantity of nickel found in an individual crystal tends to reflect the starting nickel quantity added and is well dispersed among the crystals batch compared to the iron case.

### 3.5. XNCD

To determine if the nickel compounds embedded in  $[Zn(bpy)_3](PF_6)_2$  are indeed chiral and do not simply generate racemic domains within the chiral zinc matrix, X-ray natural circular dichroism (XNCD) measurements [17,52,53] were carried on the two enantiomers

with formal proportions of  $\text{Ni}_{0.2}\text{Zn}_{0.8}(\text{bpy})_3(\text{PF}_6)_2$  at the Ni K-edge. Two crystals were mounted in an orthoaxial orientation, such that the incident X-ray beam was perpendicular to the optical  $c$ -axis, the latter is parallel to the long crystal direction (Figure S8). Absorption and XNCD spectra for the two enantiomers of  $\text{Ni}_{0.2}\text{Zn}_{0.8}(\text{bpy})_3(\text{PF}_6)_2$  are shown in Figure 5. In the absorption spectrum, the white line is observed at 8353 eV, with pre-edges at 8335.8 and 8339.2 eV. XNCD spectra for the two enantiomers appear mostly as mirror images, with the pre-edge XNCD values reaching about 0.4% of the white line absorption intensity and about 9% of the pre-edge absorption intensity. Since XNCD is sensitive to chirality and is chemically selective, the finite XNCD signals are direct proof that Ni(II) ions are sitting in non-centrosymmetric domains, i.e.,  $[\text{Ni}(\text{bpy})_3](\text{PF}_6)_2$  can adopt the conglomerate form.

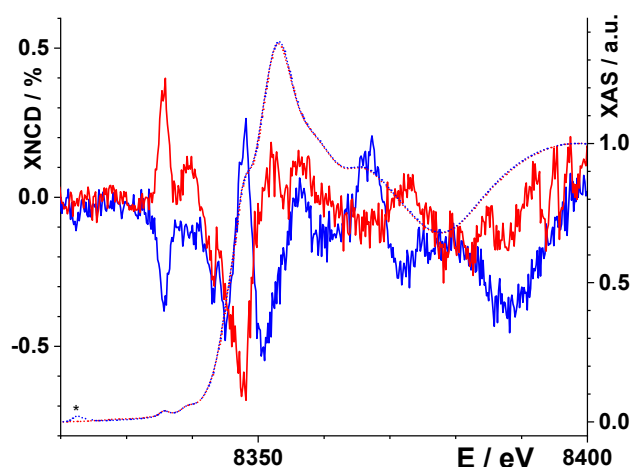


**Figure 5.** Absorption (dotted lines) and XNCD (full lines) spectra for the  $\Delta$  (in red) and  $\Lambda$  (in blue) enantiomers of  $[\text{Ni}_{0.2}\text{Zn}_{0.8}(\text{bpy})_3](\text{PF}_6)_2$ . Diffraction peaks are signaled with a \*. EDX measurements on one of the enantiomers yielded proportions of  $\text{Ni}_{0.133}\text{Zn}_{0.867}$ . Assignment of spectra to chiral configurations was made afterward, with measurements performed on two single crystals of  $[\text{Ni}_{0.1}\text{Zn}_{0.9}(\text{bpy})_3](\text{PF}_6)_2$ , the absolute configuration of which had been previously assigned by X-ray diffraction (Figure S9 in ESI).

We also performed XNCD measurements at the Fe K-edge on single crystals of both enantiomers of  $[\text{Fe}_{0.1}\text{Zn}_{0.9}(\text{bpy})_3](\text{PF}_6)_2$ , mounted in the same way. Unfortunately, the spectra were contaminated with intense diffraction peaks, which prevented a full treatment of the spectra to extract an averaged XNCD spectrum with satisfactory signal-to-noise. Nevertheless, an inspection of the pre-edge peak on a pair of spectra of opposite polarity indicates that the XNCD signal, if it exists, is clearly of limited amplitude, much more so than for the nickel compound (Figure S10).

#### 4. Conclusions

In this report, it was shown that it is possible to use conglomerate-forming matrices to enable the formation of chiral crystals of racemate-forming systems. However, the nickel and iron systems behave very differently. While there appears to be a metastable conglomerate phase for the nickel compound, which is observed in the precipitates and has previously been observed in the crystal form [31], the iron compound does not exhibit conglomerate formation in its pure form. This resistance to conglomerate formation explains why the racemic form is found with even very low iron proportions were used and why conglomerate crystals of  $[\text{Fe}_x\text{Zn}_{(x-1)}(\text{bpy})_3](\text{PF}_6)_2$  possess very low iron concentrations. This results in a heterogeneous collection of crystals with high iron content (racemates) and very low iron content (conglomerates). On the other hand, the nickel and zinc molecular alloys show a continuum of metal concentrations, allowing the formation of conglomerates with relatively high nickel content. X-ray spectroscopic measurements showed that the nickel complexes in  $[\text{Ni}_{0.13}\text{Zn}_{0.87}(\text{bpy})_3](\text{PF}_6)_2$  give rise to a circular dichroism signal,

showing that the presence of  $[\text{Zn}(\text{bpy})_3](\text{PF}_6)_2$  induces the conglomerate crystallization of  $[\text{Ni}(\text{bpy})_3](\text{PF}_6)_2$ .

**Supplementary Materials:** The following supporting information can be downloaded at: <https://www.mdpi.com/article/10.3390/chemistry5010020/s1>, Table S1: Crystal data and structure refinement for  $[\Lambda\text{-Zn}(\text{bpy})_3](\text{PF}_6)_2$  and  $[\text{rac-Ni}(\text{bpy})_3](\text{PF}_6)_2$ ; Table S2: Phase determination of  $[\text{M}(\text{bpy})_3](\text{PF}_6)_2$  crystals using single-crystal X-ray diffraction; Figure S1: Profile matching refinement (Le Bail method) for ground single crystals of  $[\text{Ni}(\text{bpy})_3](\text{PF}_6)_2$ ; Figure S2: Infrared spectra of the precipitated powders; Figure S3: Profile matching refinement (Le Bail method) for co-precipitations of  $[\text{Ni}(\text{bpy})_3](\text{PF}_6)_2$  with  $[\text{Zn}(\text{bpy})_3](\text{PF}_6)_2$ ; Figure S4: Rietveld refinement (MoK $\alpha$ 12 radiation) for ground single crystals of  $[\text{Ni}_x\text{Zn}_{(1-x)}(\text{bpy})_3](\text{PF}_6)_2$  for (a)  $x = 0.1$ , showing a unique  $\gamma$  phase (cwRp = 0.12; wR2 = 0.09), (b)  $x = 0.4$  showing a mixture of  $\gamma$  and  $\beta$  phases; Figure S5: Rietveld refinement for ground single crystals (a,c) and powders (b,d) of  $[\text{Fe}_x\text{Zn}_{(1-x)}(\text{bpy})_3](\text{PF}_6)_2$  showing a mixture of  $\gamma$  and  $\beta$  phases for (a,b):  $x = 0.1$  and %  $\beta = 7\%$  and  $1\%$ , respectively, and (c,d):  $x = 0.4$  and %  $\beta = 54\%$  and  $65\%$ , respectively; Figure S6a,b: SEM images of  $[\text{Ni}_{0.4}\text{Zn}_{0.6}(\text{bpy})_3](\text{PF}_6)_2$ . Blue crosses show the point where metal content was assayed by EDX. See Table S3 for metal assay at the labeled points; Table S3: Nickel and zinc proportions measured by EDX at the points corresponding to the blue crosses in Figure S6a,b; Figure S7: SEM images of  $[\text{Fe}_{0.5}\text{Zn}_{0.5}(\text{bpy})_3](\text{PF}_6)_2$ . Blue crosses show the point where metal content was assayed by EDX. See Table S4 for metal assay at the labeled points; Table S4: Nickel and zinc proportions measured by EDX at the points corresponding to the blue crosses in Figure S7; Figure S8: Sample mounting for X-ray Natural Circular Dichroism, crystals were glued to carbon tape pads with the c axis lying horizontal; Figure S9: Absorption (dotted lines) and XNCD (full lines) spectra for single crystals, in orthoaxial configuration respective to the beam, for the  $\Delta$  (in red) and  $\Lambda$  (in blue) enantiomers of  $\text{Ni}_{0.1}\text{Zn}_{0.9}(\text{bpy})_3(\text{PF}_6)_2$ . EDX measurements on both enantiomers gave proportions of  $\text{Ni}_{0.106}\text{Zn}_{0.894}$  for  $\Delta$  and  $\text{Ni}_{0.12}\text{Zn}_{0.88}$  for  $\Lambda$ ; Figure S10: X-ray absorption spectra for both circular polarizations of the beam (red and blue lines) on a single crystal of the  $\Delta$  enantiomer of  $\text{Fe}_{0.1}\text{Zn}_{0.9}(\text{bpy})_3(\text{PF}_6)_2$ , in orthoaxial configuration respective to the beam. Diffraction peaks present in this pair of spectra are signaled with a \*. (inset) zoom on the pre-edge region.

**Author Contributions:** Conceptualization, E.A.H.; methodology, E.A.H.; validation, M.M., E.A.H., M.G. and P.R.; formal analysis, M.M., M.G., P.R. and E.A.H.; investigation, L.R., U.S., M.M., M.G., E.A.H., P.S., P.R., F.W., A.R., E.D.-N., M.-A.A. and A.J.; data curation, P.R., M.M., M.G. and E.A.H.; writing—original draft preparation, E.A.H.; writing—review and editing, all authors; visualization, M.G., P.R., E.A.H., U.S., M.M. and L.R.; supervision, E.A.H. and E.P.; project administration, E.A.H. and E.P.; funding acquisition, E.A.H. and E.P. All authors have read and agreed to the published version of the manuscript.

**Funding:** This research was funded by the Agence Nationale de la Recherche: MaChiNaCo ANR-19-CE09-0018 and XIMTEX ANR-21-CE29-0032, the European Synchrotron Radiation Facility: CH-6094 and CH-6407, and the CNRS, the University of Bordeaux and the Bordeaux INP (recurrent funds).

**Institutional Review Board Statement:** Not applicable.

**Informed Consent Statement:** Not applicable.

**Data Availability Statement:** CCDC 2238231–2238232 contains the supplementary crystallographic data for this paper. These data can be obtained free of charge from The Cambridge Crystallographic Data Centre (CCDC) via [www.ccdc.cam.ac.uk/structures](http://www.ccdc.cam.ac.uk/structures).

**Acknowledgments:** We thank E. Lebraud and N. Daro for technical assistance and G. Duroux for encouraging discussions.

**Conflicts of Interest:** The authors declare no conflict of interest.

## References

1. Srisanga, S.; Ter Horst, J.H. Racemic Compound, Conglomerate, or Solid Solution: Phase Diagram Screening of Chiral Compounds. *Cryst. Growth Des.* **2010**, *10*, 1808–1812. [[CrossRef](#)]
2. Jacques, J.; Collet, A.; Wilen, S.H. *Enantiomers, Racemates, and Resolutions*; J. Wiley & Sons, Inc.: New York, NY, USA, 1981.
3. Pasteur, L. Mémoire Sur La Relation Qui Peut Exister Entre La Forme Cristalline et La Composition Chimique, et Sur La Cause de La Polarisation Rotatoire. *C. R. Acad. Sci. Paris* **1848**, *26*, 535–538.
4. Levilain, G.; Coquerel, G. Pitfalls and Rewards of Preferential Crystallization. *CrystEngComm* **2010**, *12*, 1983–1992. [[CrossRef](#)]

5. Sögütöglü, L.-C.; Steendam, R.R.E.; Meeke, H.; Vlieg, E.; Rutjes, F.P.J.T. Viedma Ripening: A Reliable Crystallisation Method to Reach Single Chirality. *Chem. Soc. Rev.* **2015**, *44*, 6723–6732. [[CrossRef](#)] [[PubMed](#)]
6. Levilain, G.; Eicke, M.J.; Seidel-Morgenstern, A. Efficient Resolution of Enantiomers by Coupling Preferential Crystallization and Dissolution. Part 1: Experimental Proof of Principle. *Cryst. Growth Des.* **2012**, *12*, 5396–5401. [[CrossRef](#)]
7. Coquerel, G. Preferential Crystallization. In *Novel Optical Resolution Technologies*; Sakai, K., Hirayama, N., Tamura, R., Eds.; Topics in Current Chemistry; Springer: Berlin/Heidelberg, Germany, 2007; pp. 1–51. ISBN 978-3-540-46320-7.
8. Binev, D.; Seidel-Morgenstern, A.; Lorenz, H. Continuous Separation of Isomers in Fluidized Bed Crystallizers. *Cryst. Growth Des.* **2016**, *16*, 1409–1419. [[CrossRef](#)]
9. Dunn, A.S.; Szilagy, B.; ter Horst, J.H.; Nagy, Z.K. Enabling Mechanical Separation of Enantiomers through Controlled Batchwise Concomitant Crystallization: Digital Design and Experimental Validation. *Cryst. Growth Des.* **2020**, *20*, 7726–7741. [[CrossRef](#)]
10. Eicke, M.J.; Levilain, G.; Seidel-Morgenstern, A. Efficient Resolution of Enantiomers by Coupling Preferential Crystallization and Dissolution. Part 2: A Parametric Simulation Study to Identify Suitable Process Conditions. *Cryst. Growth Des.* **2013**, *13*, 1638–1648. [[CrossRef](#)]
11. Galan, K.; Eicke, M.J.; Elsner, M.P.; Lorenz, H.; Seidel-Morgenstern, A. Continuous Preferential Crystallization of Chiral Molecules in Single and Coupled Mixed-Suspension Mixed-Product-Removal Crystallizers. *Cryst. Growth Des.* **2015**, *15*, 1808–1818. [[CrossRef](#)]
12. Galland, A.; Dupray, V.; Berton, B.; Morin-Grognon, S.; Sanselme, M.; Atmani, H.; Coquerel, G. Spotting Conglomerates by Second Harmonic Generation. *Cryst. Growth Des.* **2009**, *9*, 2713–2718. [[CrossRef](#)]
13. Newman, A.C.D.; Powell, H.M. The Spontaneous Optical Resolution of Solvated Tri-*o*-Thymotide. *J. Chem. Soc.* **1952**, 718, 3747–3751. [[CrossRef](#)]
14. Harfouche, L.C.; Brandel, C.; Cartigny, Y.; Ter Horst, J.H.; Coquerel, G.; Petit, S. Enabling Direct Preferential Crystallization in a Stable Racemic Compound System. *Mol. Pharm.* **2019**, *16*, 4670–4676. [[CrossRef](#)] [[PubMed](#)]
15. Mbodji, A.; Gbabode, G.; Sanselme, M.; Cartigny, Y.; Couvrat, N.; Leeman, M.; Dupray, V.; Kellogg, R.M.; Coquerel, G. Evidence of Conglomerate with Partial Solid Solutions in Ethylammonium Chloxyphos. *Cryst. Growth Des.* **2020**, *20*, 2562–2569. [[CrossRef](#)]
16. Mbodji, A.; Gbabode, G.; Sanselme, M.; Couvrat, N.; Leeman, M.; Dupray, V.; Kellogg, R.M.; Coquerel, G. Family of Conglomerate-Forming Systems Composed of Chloxyphos and Alkyl-Amine. Assessment of Their Resolution Performances by Using Various Modes of Preferential Crystallization. *Cryst. Growth Des.* **2019**, *19*, 5173–5183. [[CrossRef](#)]
17. Cortijo, M.; Valentín-Pérez, Á.; Rogalev, A.; Wilhelm, F.; Sainctavit, P.; Rosa, P.; Hillard, E.A. Rapid Discrimination of Crystal Handedness by X-Ray Natural Circular Dichroism (XNCD) Mapping. *Chem. Eur. J.* **2020**, *26*, 13363–13366. [[CrossRef](#)]
18. Atzori, M.; Ludowieg, H.D.; Valentín-Pérez, Á.; Cortijo, M.; Breslavetz, I.; Paillet, K.; Rosa, P.; Train, C.; Autschbach, J.; Hillard, E.A.; et al. Validation of Microscopic Magneto-chiral Dichroism Theory. *Sci. Adv.* **2021**, *7*, eabg2859. [[CrossRef](#)]
19. Sessoli, R.; Boulon, M.-E.; Caneschi, A.; Mannini, M.; Poggini, L.; Wilhelm, F.; Rogalev, A. Strong Magneto-Chiral Dichroism in a Paramagnetic Molecular Helix Observed by Hard X-rays. *Nat. Phys.* **2015**, *11*, 69–74. [[CrossRef](#)]
20. Train, C.; Nuida, T.; Gheorghe, R.; Gruselle, M.; Ohkoshi, S. Large Magnetization-Induced Second Harmonic Generation in an Enantiopure Chiral Magnet. *J. Am. Chem. Soc.* **2009**, *131*, 16838–16843. [[CrossRef](#)]
21. Atzori, M.; Breslavetz, I.; Paillet, K.; Inoue, K.; Rikken, G.L.J.A.; Train, C. A Chiral Prussian Blue Analogue Pushes Magneto-Chiral Dichroism Limits. *J. Am. Chem. Soc.* **2019**, *141*, 20022–20025. [[CrossRef](#)]
22. Bernal, I.; Kauffmann, G.B. The Spontaneous Resolution of Cis-Bis(Ethylenediamine)Dinitrocobalt(III) Salts: Alfred Werner's Overlooked Opportunity. *J. Chem. Educ.* **1987**, *64*, 604–610. [[CrossRef](#)]
23. Björemark, P.M.; Jönsson, J.; Håkansson, M. Absolute Asymmetric Synthesis: Viedma Ripening of [Co(Bpy)<sub>3</sub>]<sup>2+</sup> and Solvent-Free Oxidation to [Co(Bpy)<sub>3</sub>]<sup>3+</sup>. *Chem. Eur. J.* **2015**, *21*, 10630–10633. [[CrossRef](#)] [[PubMed](#)]
24. Saha, M.K.; Ramanujam, R.; Bernal, I.; Fronczek, F.R. The Phenomenon of Conglomerate Crystallization. Part 57. Control of the Crystallization Behavior by the Choice of the Counter Ion. Part 9. The Stereochemistry and Crystallization Architecture of [(3,2,3-Tet)Co(N<sub>3</sub>)<sub>2</sub>]X (X = Cl(I), Br(II), I(III), NO<sub>3</sub> (IV), and PF<sub>6</sub> (V)). *Cryst. Growth Des.* **2002**, *2*, 205–212.
25. Neill, D.; Riley, M.J.; Kennard, C.H.L. Tris(Ethylenediamine-N,N')Zinc(II) Dinitrate. *Acta Cryst. C* **1997**, *53*, 701–703. [[CrossRef](#)]
26. Caughlan, C.N.; Emerson, K. Crystal and Molecular Structure of Tris(Ethylenediamine)Nickel(II) Sulfate, Ni(NH<sub>2</sub>CH<sub>2</sub>CH<sub>2</sub>NH<sub>2</sub>)<sub>3</sub>SO<sub>4</sub>. *Inorg. Chem.* **1970**, *9*, 2421–2424. [[CrossRef](#)]
27. Deisenroth, S. CSD Structure Code YEGLUR, Untersuchung der Folgeprozesse des <sup>57</sup>Co-Kernzerfalls in der Komplexverbindung [<sup>57</sup>Co/Mn(bipy)<sub>3</sub>](PF<sub>6</sub>)<sub>2</sub>. Ph.D. Thesis, University of Mainz Institut für Anorganische Chemie und Analytische Chemie, Mainz, Germany, 1996.
28. Archer, C.M.; Dilworth, J.R.; Thompson, R.M.; McPartlin, M.; Povey, D.C.; Kelly, J.D. The Synthesis and Reactivity of a New Technetium(III) Precursor. The Crystal Structures of [TcCl<sub>3</sub>(MeCN){P(C<sub>6</sub>H<sub>4</sub>Me-3)<sub>3</sub>}<sub>2</sub>] and [Tc(Bipy)<sub>3</sub>]<sup>2+</sup> (Bipy = 2,2'-Bipyridine). *J. Chem. Soc. Dalton Trans.* **1993**, *3*, 461–466. [[CrossRef](#)]
29. Mentş, A.; Singh, K. Tris(2,2'-Bipyridine-K<sub>2</sub>N,N')Cobalt(II) Bis (Hexa fluoridophosphate). *Acta Cryst. E* **2013**, *69*, m58. [[CrossRef](#)]
30. Wang, L.; Yang, Y.; Huang, W. Tris(2,2'-Bipyridyl-K<sub>2</sub>N,N')Copper(II) Hexa fluoridophosphate. *Acta Cryst. E* **2007**, *63*, m835–m836. [[CrossRef](#)]
31. Breu, J.; Domel, H.; Stoll, A. Racemic Compound Formation versus Conglomerate Formation with [M(Bpy)<sub>3</sub>](PF<sub>6</sub>)<sub>2</sub> (M = Ni, Zn, Ru); Molecular and Crystal Structures. *Eur. J. Inorg. Chem.* **2000**, *2000*, 2401–2408. [[CrossRef](#)]

32. Dick, S. Crystal structure of tris(2,2'-bipyridine)iron(II) bis(hexafluorophosphate),  $(C_{10}H_8N_2)_3Fe(PF_6)_2$ . *Z. Für Krist. New Cryst. Struct.* **1998**, *213*, 370. [[CrossRef](#)]
33. Rillema, D.P.; Jones, D.S.; Woods, C.; Levy, H.A. Comparison of the Crystal Structures of Tris Heterocyclic Ligand Complexes of Ruthenium(II). *Inorg. Chem.* **1992**, *31*, 2935–2938. [[CrossRef](#)]
34. Rillema, D.P.; Jones, D.S. Structure of Tris(2,2'-Bipyridyl)Ruthenium(II) Hexafluorophosphate,  $[Ru(Bipy)_3][PF_6]_2$ ; X-Ray Crystallographic Determination. *J. Chem. Soc., Chem. Commun.* **1979**, *19*, 849–851. [[CrossRef](#)]
35. Bouzaid, J.; Schultz, M.; Lao, Z.; Bartley, J.; Bostrom, T.; McMurtrie, J. Supramolecular Selection in Molecular Alloys. *Cryst. Growth Des.* **2012**, *12*, 3906–3916. [[CrossRef](#)]
36. Constable, E.C.; Raithby, P.R.; Smit, D.N. The X-Ray Crystal Structure of Tris (2,2'-Bipyridine)Osmium(II) Hexafluorophosphate. *Polyhedron* **1989**, *8*, 367–369. [[CrossRef](#)]
37. Richter, M.M.; Scott, B.; Brewer, K.J.; Willett, R.D. Crystal and Molecular Structure of Tris(2,2'-Bipyridyl)Osmium(II) Bis(Hexafluorophosphate). *Acta Cryst. C* **1991**, *47*, 2443–2444. [[CrossRef](#)]
38. Biner, M.; Buergi, H.B.; Ludi, A.; Roehr, C. Crystal and Molecular Structures of  $[Ru(Bpy)_3](PF_6)_3$  and  $[Ru(Bpy)_3](PF_6)_2$  at 105 K. *J. Am. Chem. Soc.* **1992**, *114*, 5197–5203. [[CrossRef](#)]
39. Hadadzadeh, H.; Mansouri, G.; Rezvani, A.; Khavasi, H.R.; Skelton, B.W.; Makha, M.; Charati, F.R. Mononuclear Nickel(II) Complexes Coordinated by Polypyridyl Ligands. *Polyhedron* **2011**, *30*, 2535–2543. [[CrossRef](#)]
40. Brewer, B.; Brooks, N.R.; Abdul-Halim, S.; Sykes, A.G. Differential metathesis reactions of 2,2'-bipyridine and 1,10-phenanthroline complexes of cobalt(II) and nickel(II): Cocrystallization of ionization isomers  $\{[cis-Ni(phen)_2(H_2O)_2][cis-Ni(phen)_2(H_2O)Cl]\}(PF_6)_3 \cdot 4.5H_2O$ , and a Synthetic Route to Asymmetric Tris-Substituted Complexes. *J. Chem. Crystallogr.* **2003**, *12*, 651–662.
41. Breu, J.; Domel, H.; Norrby, P.-O. Racemic Compound Formation versus Conglomerate Formation with  $[M(Bpy)_3](PF_6)_2$  (M = Ni, Zn, Ru); Lattice Energy Minimisations and Implications for Structure Prediction. *Eur. J. Inorg. Chem.* **2000**, *2000*, 2409–2419. [[CrossRef](#)]
42. Habib, F.; Lin, P.-H.; Long, J.; Korobkov, I.; Wernsdorfer, W.; Murugesu, M. The Use of Magnetic Dilution to Elucidate the Slow Magnetic Relaxation Effects of a Dy<sub>2</sub> Single-Molecule Magnet. *J. Am. Chem. Soc.* **2011**, *133*, 8830–8833. [[CrossRef](#)]
43. Flores Gonzalez, J.; Douib, H.; Le Guennic, B.; Pointillart, F.; Cador, O. Ytterbium-Centered Isotopic Enrichment Leading to a Zero-Field Single-Molecule Magnet. *Inorg. Chem.* **2021**, *60*, 540–544. [[CrossRef](#)]
44. Balogh, M.C. New Luminescent Materials, Bio-Inspired and Recyclable, Based on Lanthanide Complexes. Ph.D. Thesis, Université de Lyon, Lyon, France, 2016.
45. Bruker. *SAINT+*; Bruker AXS Inc.: Madison, WI, USA, 2012.
46. Sheldrick, G.M. *SHELXS 97*, Program for the Solution of Crystal Structure. University of Göttingen: Göttingen, Germany, 1990.
47. Dolomanov, O.V.; Bourhis, L.J.; Gildea, R.J.; Howard, J.a.K.; Puschmann, H. OLEX2: A Complete Structure Solution, Refinement and Analysis Program. *J. Appl. Cryst.* **2009**, *42*, 339–341. [[CrossRef](#)]
48. Sheldrick, G.M. Crystal Structure Refinement with *SHELXL*. *Acta Cryst. C* **2015**, *71*, 3–8. [[CrossRef](#)] [[PubMed](#)]
49. Petříček, V.; Dušek, M.; Palatinus, L. Crystallographic Computing System JANA2006: General Features. *Zeitschrift für Krist. Cryst. Mater.* **2014**, *229*, 345–352. [[CrossRef](#)]
50. Groom, C.R.; Bruno, I.J.; Lightfoot, M.P.; Ward, S.C. The Cambridge Structural Database. *Acta Cryst. B* **2016**, *72*, 171–179. [[CrossRef](#)] [[PubMed](#)]
51. Kundu, N.; Mandal, D.; Chaudhury, M.; Tiekink, E.R.T. Luminescence Characteristics and X-ray Crystal Structure of  $[Cd(Bipy)_3][PF_6]_2$  (Bipy = 2,2'-Bipyridine). *Appl. Organomet. Chem.* **2005**, *19*, 1268–1270. [[CrossRef](#)]
52. Stewart, B.; Peacock, R.D.; Alagna, L.; Prosperi, T.; Turchini, S.; Goulon, J.; Rogalev, A.; Goulon-Ginet, C. Circular Dichroism at the Edge: Large X-Ray Natural CD in the 1s → 3d Pre-Edge Feature of  $2[Co(En)_3Cl_3] \cdot NaCl \cdot 6H_2O$ . *J. Am. Chem. Soc.* **1999**, *121*, 10233–10234. [[CrossRef](#)]
53. Srinivasan, A.; Cortijo, M.; Bulicanu, V.; Naim, A.; Clerac, R.; Sainctavit, P.; Rogalev, A.; Wilhelm, F.; Rosa, P.; Hillard, E.A. Enantiomeric Resolution and X-ray Optical Activity of a Tricobalt Extended Metal Atom Chain. *Chem. Sci.* **2018**, *9*, 1136–1143. [[CrossRef](#)]

**Disclaimer/Publisher's Note:** The statements, opinions and data contained in all publications are solely those of the individual author(s) and contributor(s) and not of MDPI and/or the editor(s). MDPI and/or the editor(s) disclaim responsibility for any injury to people or property resulting from any ideas, methods, instructions or products referred to in the content.